Role of particle size on the multicycle calcium looping activity of limestone for thermochemical energy storage

Jonatan D. Durán-Martín [a,*], Pedro E. Sánchez Jimenez [a,*], José M. Valverde [b], Antonio Perejón [a,c], Juan Arcenegui-Troya [a], Pablo García Triñanes [d], Luis A. Pérez Maqueda [a]

[a] Instituto de Ciencia de Materiales de Sevilla, C.S.I.C.-Universidad de Sevilla, C. Américo Vespucio n°49, 41092 Sevilla, Spain
[b] Faculty of Physics, University of Seville, Avenida Reina Mercedes s/n, Sevilla, Spain
[c] Departamento de Química Inorgánica, Facultad de Química, Universidad de Sevilla, Sevilla, Spain
[d] Flow, Heat and Reaction Engineering Group, FHRENG, Chemical Engineering Division, School of Engineering, University of Greenwich, United Kingdom

HIGHLIGHTS

- Thermal energy performance of narrow particle size distribution limestones is studied.
- Multicyclic activity is better for small particles under all the different studied conditions.
- This effect is particularly relevant for particles smaller than 15 μm median particle size.
- Particle size effect is not relevant for particles between 15 and 900 μm.

GRAPHICAL ABSTRACT
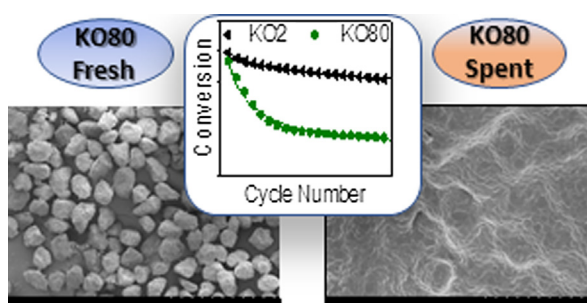
ABSTRACT

The calcium looping process, based on the reversible reaction between $CaCO_3$ and CaO, is recently attracting a great deal of interest as a promising thermochemical energy storage system to be integrated in Concentrated Solar Power plants (CaL-CSP). The main drawbacks of the system are the incomplete conversion of CaO and its sintering-induced deactivation. In this work, the influence of particle size in these deactivation mechanisms has been assessed by performing experimental multicycle tests using standard limestone particles of well-defined and narrow particle size distributions. The results indicate that CaO multicycle conversion benefits from the use of small particles mainly when the calcination is carried out in helium at low temperature. Yet, the enhancement is only significant for particles below 15 μm. On the other hand, the strong sintering induced by calcining in CO_2 at high temperatures makes particle size much less relevant for the multicycle performance. Finally, SEM imaging reveals that the mechanism responsible for the loss of activity is mainly pore-plugging when calcination is performed in helium, whereas extensive loss of surface area due to sintering is responsible for the deactivation when calcination is carried out in CO_2 at high temperature.

© 2019 The Authors. Published by Elsevier B.V. on behalf of Cairo University. This is an open access article under the CC BY-NC-ND license (http://creativecommons.org/licenses/by-nc-nd/4.0/).

Introduction

Global warming is one of the main challenges faced in this 21st century. The main cause is CO_2 emissions from anthropogenic origin, which are mainly produced by the combustion of fossil fuels

[1]. Despite increasing effort in developing environmentally friendly technologies based on renewable energy sources, fossil fuel power plants still account for a significant share of the overall energy mix. Thus, greenhouse gas emissions from this type of facilities are still at unacceptable levels [2]. The main alternative renewable energy sources to replace fossil fuel power plants are wind and solar. Nonetheless, these technologies share an important shortcoming in their inability to provide a constant energy supply due to the intrinsic intermittency of wind and sunlight. Concentrated solar power plants (CSP) offer the possibility of integrating grid energy production with large-scale thermal energy storage (TES) thereby achieving dispatchability [3,4]. TES systems in commercial CSP plants include steam accumulators and high specific heat molten salts [4–6]. However, storing the heat produced by direct solar radiation as chemical energy entail several advantages [7,8]. For instance, the long-term storage of the products without radiative heat losses becomes possible. At the same, the continuous energy consumption required to maintain the salts in molten state is avoided [9]. Finally, Current molten salts are limited to about 560 °C to avoid degradation, thereby limiting the maximum attainable efficiency [10]. Achieving higher temperatures could boost the efficiency of the thermodynamic power cycle as the difference between charge and discharge temperature becomes larger [8,11]. Finally, exergy efficiency is enhanced due to the larger energy densities provided by reaction enthalpies as compared to sensible and latent heats [8,12,13]. Among several chemical looping alternatives, the calcium looping (CaL) process has attracted a great deal of interest as a very promising system for thermochemical energy storage (TCES) since it displays several advantages such as low cost, high reaction temperature, acceptable reversibility and high energy density [14–16].

In the last decades, the CaL process has been explored as an avenue to mitigate CO_2 emissions in fossil fuel power plants and cement manufacture facilities since it constitutes an effective technology for CO_2 capture and storage (CCS). The CaL process is based on the reversible calcination of $CaCO_3$ into CaO [17]:

$$CaCO_3(s) \rightleftharpoons CaO(s) + CO_2(g) \ \Delta H_r^0 = 178 \ kJ \cdot mol^{-1} \qquad (1)$$
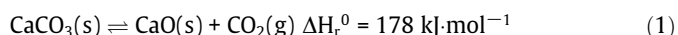
This reaction has been widely studied since it is a fundamental step in cement production. Thus, it is relatively feasible to establish the optimum conditions for direct and reverse reaction depending on the application. $CaCO_3$ is inexpensive and abundant in the form of different minerals (limestone, marble, dolomite, etc) [18,19]. It exhibits a high reaction enthalpy that allows for a high theoretical energy density, ranging from 1 to 4 GJ/m^3 depending on the author and estimation method [12,13,20]. In the last years, several schemes regarding the integration of the CaL process in CSP plants (CaL-CSP) [14,21–23]. These contemplate the calcination of $CaCO_3$ using direct solar radiation as heat source. Solar radiation can impinge directly on the storage material or it can be used to heat up the external walls of a solar particle receiver [14,24]. Stored energy is recovered through the reverse exothermic solid-gas reaction between CaO and CO_2 at higher temperatures in the carbonator. Excess CO_2 out of the carbonator is then circulated to power a CO_2 turbine and produce electricity on demand. The high temperature of the working gas would ensure higher efficiency as compared with that of TES plants [16].

The CaL process exhibits two significant drawbacks that penalize its large-scale implementation, the incomplete conversion of CaO and its progressive deactivation along the successive carbonation/calcination cycles [14,25]. The decay in CaO conversion is generally attributed to the extensive sintering and loss of surface area that occur at the high temperature and high CO_2 partial pressure required [26–28]. Moreover, it has been observed that, when calcination is carried out in inert gas, a blocking $CaCO_3$ layer rapidly forms on the CaO particles surface during the subsequent carbonation. This pore-plugging layer severely hinders further diffusion of CO_2 molecules and prevents achieving complete conversion [29–31]. Therefore, the optimum conditions for CSP storage would be those that maximize the discharge temperature in order to improve the efficiency of the thermodynamic cycle while avoiding excessive sorbent deactivation. Recent studies have shown that can be achieved by carrying out the calcination at the lowest possible temperature in inert gas, and the carbonation at the maximum attainable temperature in CO_2, normally about 950 °C [32,33]. However, pressurized carbonation (at ~3 bars) would allow to further extend the maximum carbonation temperature [16,34].

Being one of the relevant challenges to overcome towards making the CaL-CSP technology attractive at industrial level, a number of strategies have been devised to reduce CaO deactivation. Thus, it is well known that crystallinity [35], particle size [18,36], morphology [37,38] and the inclusion of additives [19,39] have a strong influence on Ca-based multicycle performance. Regarding the impact of particle size, it has been observed that large or highly crystalline particles exhibit substantially slower decarbonation kinetics, thereby requiring higher temperatures for the complete regeneration of CaO in short residence times [40]. Additionally, carbonation in large particles is hindered by pore diffusion and pore-plugging [30,41,42]. On the other hand, small particles exhibits faster calcination at lower temperatures, what eventually results in improved long term recyclability [18]. Moreover, the use of small particles would facilitate the integration with solar energy and decrease the cost in materials for constructing the solar receiver [43]. However, small particles are difficult to handle in industrial processes based on fluidised bed reactors. Trajectories and residence times of particles in cyclones strongly depend on their size while collection efficiency decays markedly for particles with sizes below 10 μm [44,45]. Thus, the usual particle size lower limit to ensure an acceptable efficiency of cyclones is about 50 μm. Overall, the optimum particle size in pilot plants based on fluidised bed reactors has been found to lie within the 100–300 μm range [46,47].

Despite its importance, the influence of particle size in CaL-CSP has yet to be explored in sufficient detail since most published works use material with very wide particle size distributions. In this study, multicycle CaL-CSP experiments have been carried out using limestone sample sets with well-defined particle sizes, ranging from small 4-μm particles to large 900-μm particles. At the same time, Scanning Electron Microscopy (SEM) has been used to observe the morphological changes undergone by the material during consecutive carbonation and calcination cycles, in order to assess the mechanism responsible of the loss of activity. The results herein shed light on the relationship between particle size, extent of conversion after each cycle and deactivation after repeated carbonation and calcination cycles. Two different CaL-CSP operation schemes have been considered. First, the calcination stage is carried out in helium (CSP-He) as originally conceived in [32]. This procedure takes advantage of the high thermal conductivity of helium and the high diffusivity of CO_2 in this gas to favour the calcination process so that full decarbonation is achieved in short residence times at temperatures as low as 700–750 °C. However, employment of helium at industrial scale entails technical issues such as high cost, gas losses and the necessity of gas separation from CO_2 after calcination. Thus, the tests have also been carried out using an alternative operation scheme in CO_2 closed cycle. This second integration scheme would be less complicated to implement technically but would entail raising the calcination temperature up to 950 °C.

Table 1
PSD data of limestone samples. Adapted from [48].

Sample		KO2	KO4	KO15	KO30	KO80	KO900
Particle size (μm)	d_{10}	0.78	1.6	12	21	39	738
	d_{50}	2.22	4.42	19	30	71	938
	d_{90}	4.15	8.25	28	43	106	1148
Span	$(d_{90}-d_{10})/d_{50}$	1.52	1.50	0.84	0.73	0.94	0.44

Experimental

Materials

The samples used in this work were limestone from standard Eskal series supplied by KSL Staubtechnik GmbH (Germany). The Eskal series are widely used in powder technology studies as standards for calibration of equipment and testing. Particle size distributions were determined by laser diffraction as reported in [48]. Five different samples with a well-defined average particle size were studied (2, 4, 15, 30 and 80 μm). An additional sample with larger particle size, ranging from 700 to 1000 μm, was also tested. Samples will be referred hereafter as KO2, KO4, KO15, KO30, KO80 and KO900. PSD data are listed in Table 1 while frequency distributions of particle sizes for all samples are plotted in Fig. 1.

Methods

Multicycle calcination/carbonation tests were carried out in a TA instrument Q5000IR TG analyzer equipped with a IR furnace composed of a SiC reaction chamber heated by IR lamps that allows high cooling and heating rates up to 300 °C·min^{-1}. Such rates are necessary to emulate realistic CaL conditions in which the material is rapidly circulated between carbonator and calciner at different temperatures. All tests were run using small sample masses ($\approx$10 mg) in order to avoid interfering mass and heat transfer phenomena as well as to facilitate exchanges with the surrounding atmosphere. The reaction chamber has a volume of just 20 cm^3. According to process simulations, the maximum efficiency in CaL-CSP plants, not considering pressurized conditions, is achieved when the carbonation reaction takes place in a high CO$_2$ concentration environment at about 850 °C [16]. Considering this, the samples were tested according to the energy storage conditions described below:

CSP-He

CSP-He experiments begin with a calcination step (from room temperature to 750 °C at 300 °C·min^{-1}) under He atmosphere followed by a 5-min isothermal stage. After this first calcination,
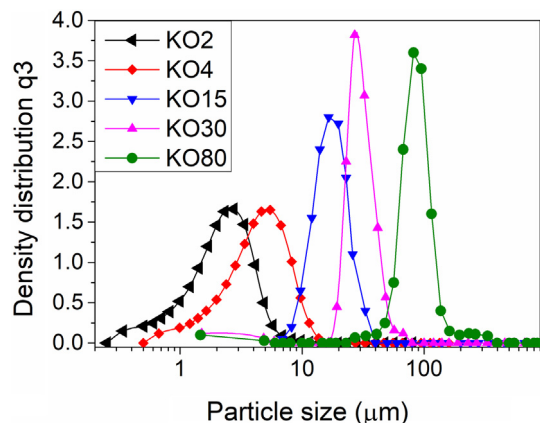
carbonation is initiated in pure CO$_2$ atmosphere by increasing the temperature at a rate of 300 °C·min^{-1} up to 850 °C, and keeping this temperature for 5 min. Then, a new calcination stage is triggered by reducing the temperature at 300 °C·min^{-1} down to 750 °C under He, followed by 5-min isotherm. An intermediate step is introduced after calcination by decreasing the temperature down to 300 °C under He for 2 min. This stage is intended to simulate the extraction of sensible heat from reaction products after calcination. After this cooling step a new cycle is started, for a total of 20 carbonation/calcination cycles.

CSP-CO$_2$

CSP-CO$_2$ experiments begin with a precalcination stage (from room temperature to 950 °C at 300 °C·min^{-1}, held for 5 min) in high CO$_2$ concentration (95% CO$_2$/5% air vol/vol). Precalcination is followed by a carbonation stage without changing the atmosphere by quickly decreasing the temperature down to 850 °C at 300 °C·min^{-1} and maintaining this temperature for 5 min. A total of 20 carbonation/calcination cycles were run in these tests.

SEM micrographs of gold-sputtered samples (40 mA, 30 s) were taken employing a Hitachi S4800 FEG microscope at 5 kV.

Nitrogen adsorption–desorption isotherms were measured using an ASAP2420 (Micromeritics) instrument. Samples degassing was carried out at 300 °C for 2 h. Total surface areas (S_{BET}) were determined using the BET equation. In order to prepare the amount of sample needed for BET measurements, a tubular furnace was employed. Samples were prepared in small batches (300 mg of CaCO$_3$ at a time) to minimize mass and heat transfer phenomena during the calcination and carbonation reactions. The experimental schemes were similar to that described in B.1 and B.2 but calcination times had to be extended to 30 min to ensure complete decarbonation.

Results and discussion

Multicycle conversion

Fig. 2 shows, as an example, the complete thermograms recorded in the multicycle tests in both CSP-He and CSP-CO$_2$ conditions for the KO30 sample. The main implication of the latter conditions is that calcination temperature needs to be raised up to 950 °C in order to achieve complete decarbonation within the scheduled 5-min step, as compared to just 750 °C required when helium is used as carrier gas. Fig. 3 includes a detail of the 1st, 10th and 20th cycles, highlighting the differences in the fast kinetic-driven and diffusion driven carbonation phases depending on particle size and operation scheme. It has been amply reported that the carbonation in CaL processes proceeds through two well differentiated stages [42]; first a rapid reaction controlled phase that depends on CaO available surface which is abruptly followed by a much slower diffusion controlled phase that triggers once a barrier layer composed of CaCO$_3$ product forms, hindering further diffusion of CO$_2$ molecules [49]. The diffusion controlled stage becomes rate-limiting step once the CaCO$_3$ product layer reaches the critical value that depends on reaction conditions [31].

Fig. 3 illustrates the influence of particle size, cycle number and operation scheme on the relative importance of fast reaction-
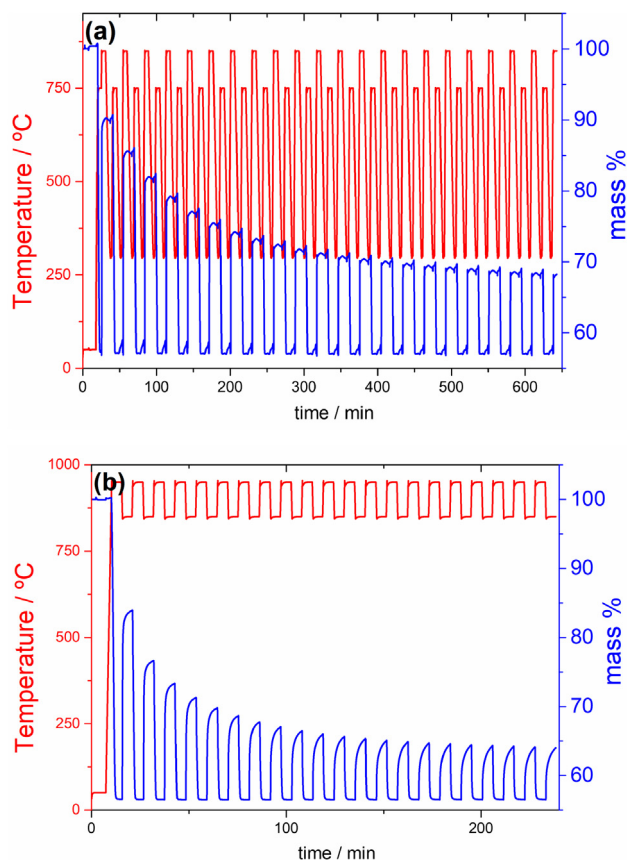

Fig. 1. Frequency distributions of particle sizes (q3) measured for all tested samples.

Fig. 2. Multicycle thermograms corresponding to KO30 sample in CaL tests carried out in (a) CSP-He and (b) CSP-CO$_2$ conditions.

controlled and slow diffusion-controlled carbonation stages. It can be inferred from the plots in Fig. 3a and b that in CSP-He the carbonation reaction is mainly determined by the fast reaction regime, with negligible CO$_2$ uptake during the subsequent diffusion-controlled stage. This behaviour serves to highlight the pore-plugging phenomenon, since the rapid formation of a blocking CaCO$_3$ layer limits further CO$_2$ diffusion to the porous interior of the particle. Therefore, in CSP-He conditions, the conversion at each cycle depends mostly on the extension of the carbonation achieved during the fast stage since the relative contribution of diffusion-controlled carbonation is very small. In contrast, the relative contribution of each carbonation phase differs in CSP-CO$_2$. As shown in Fig. 3c and d, in CSP-CO$_2$ the weight of diffusion-controlled carbonation is much more relevant. The extension of the reaction-controlled stage during the first recarbonation is roughly independent of the particle size save for the largest KO900 particles, which displays an unusual behaviour that might be related to its substantially slower decarbonation kinetics. However, the diffusion-controlled regime is promoted in smaller particles. Finally, Fig. 3d shows a marked decrease of the reaction-controlled carbonation with the cycle number. After 10 cycles, the carbonation is mainly diffusive, what implies that the CaO is heavily sintered (Fig. 3d). Another important issue, illustrated in Fig. 4, is decarbonation kinetics. The measured reaction rate is much faster when calcining at CSP-CO$_2$ conditions due to the higher employed temperatures.

The CaO conversion (X) is used to quantitatively compare the performance of different materials and reaction conditions. This parameter provides a measure of the extension of the reaction at any given cycle. It is defined as the ratio of the mass of CaO converted in the carbonation stage of each cycle to the total CaO mass before carbonation [50]. In order to extrapolate at long term and determine the residual conversion after a large number of cycles,
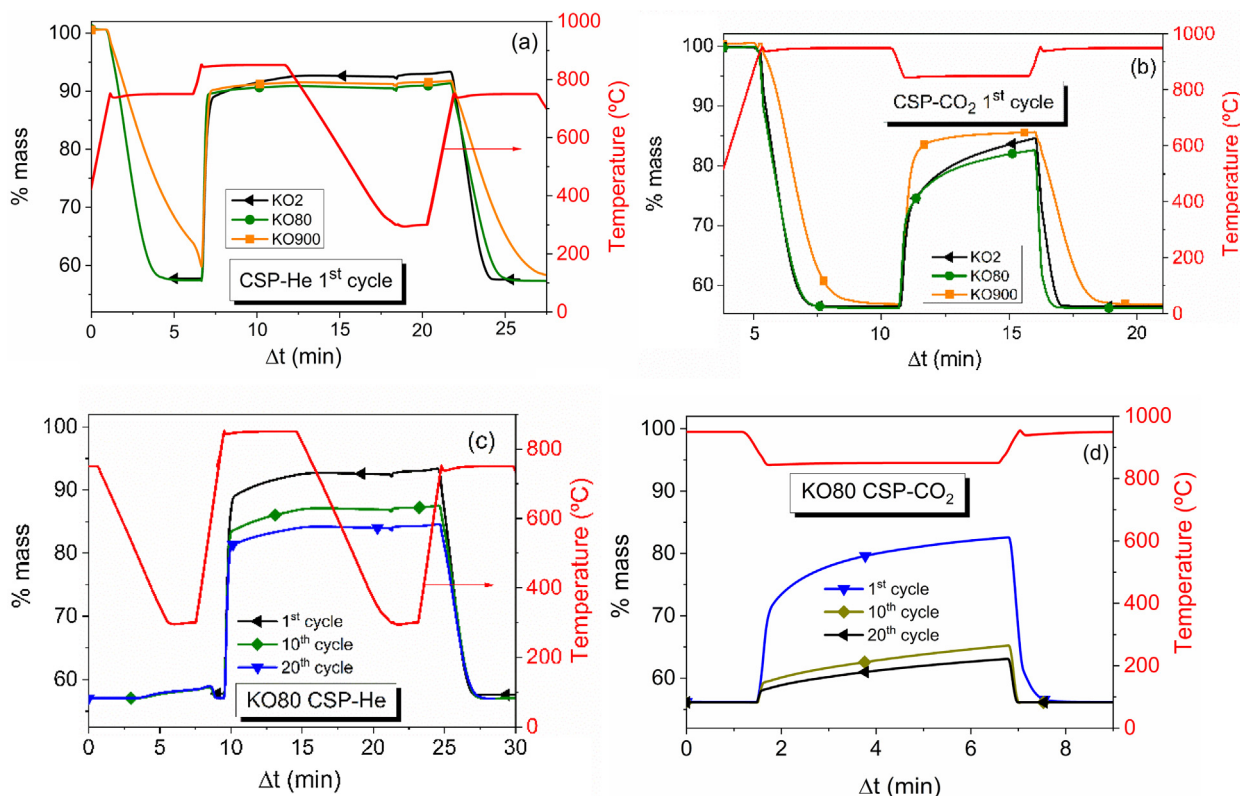

Fig. 3. Time evolution of temperature and mass % for the 1st calcination/carbonation cycle in (a) CSP-He and (b) CSP-CO$_2$ conditions for different particle sizes and comparison of 1st, 10th and 20th cycle for the KO80 sample in (c) CSP-He and (d) CSP-CO$_2$.
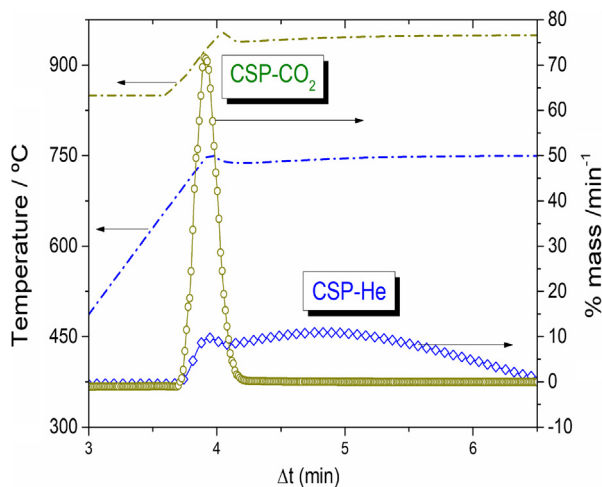
Fig. 4. Comparison of the decarbonation rate of KO80 sample measured at the 4th cycle under both CSP-He and CSP-CO$_2$.

the conversion plots can be fitted by the following semi-empirical equation [26,50]:

$$X_N = Xr + \left(\frac{X1}{K(N-1) + \left(1 - \frac{Xr}{X1}\right)^{-1}} \right) \tag{2}$$

where Xr is the residual conversion, which converges asymptotically after a large number of cycles), K is the so-called deactivation constant, X_1 is the conversion at the first cycle and X_{20} the conversion at the 20th cycle. Best fitting parameters are included in Table 2. In summary, the data show that conversion achieved in CSP-He is in all cases higher than the conversion achieved in CSP-CO$_2$. However, the difference in residual conversion, the really relevant parameter for industrial purposes, is only significant for KO2 and KO4; the two smaller particle sizes tested.

Fig. 5 includes the comparison of the CaO conversion as a function of the cycle number obtained for each particle size and for both CSP-He and CSP-CO$_2$ reaction conditions. The largest particle size tested (KO900) in CSP-He conditions displays a low conversion during the first carbonation. That occurs because the first calcination is incomplete since decarbonation kinetics are very slow for such large particle sizes [30]. As expected, the decay of CaO conversion is more pronounced for larger particles since they are more liable to deactivation by pore-plugging [30]. Also, cycling stability is noticeably impaired in CSP-CO$_2$ due to the significantly harsher calcination conditions (950 °C in pure CO$_2$) thereby favouring the loss of reactive surface due to sintering [27]. However, the detrimental effect of using large particles is much more important in CSP-He, with a substantial drop in residual conversion from 0.55 to 0.15 as the average particle size (d_{50}) increases from 2 to 900 μm respectively. On the other hand, the handicap of using large particles is less significant in CSP-CO$_2$ conditions. In such case, the residual CaO conversion drops from 0.17 to just 0.07 for the same average size increase (from 2 and 900 μm). It is nonetheless surprising the limited influence of particle size on conversion observed in CSP-He over a minimum threshold value. Thus, multi-cycle conversion performance only improves substantially for average sizes below 15 μm. This entails significant implications towards any prospective application at large scale. Since fine particles below 50 μm are cohesive and cannot be fluidised in practical applications and long term conversion of large particles is not significantly worse in CSP-CO$_2$ conditions, our work suggests the technically simpler closed CO$_2$ system might eventually be more advantageous, at least from the point of view of materials performance.

Influence of particle size and reaction conditions on sample morphology

In order to gain a better understanding of the influence of particle size on multicycle performance, the morphological changes undergone during carbonation and calcination stages have been

Table 2
CaO conversion values (at 1st, 20th and residual conversion) and deactivation constants for limestone samples at CSP-He and CSP-CO$_2$ conditions. ΔX_r is the difference in residual conversions estimates for each particle size and conditions employed.

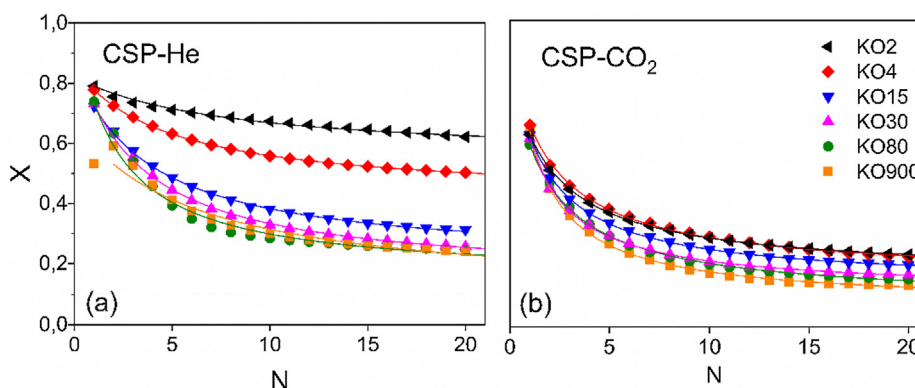| Sample	KO2		KO4		KO15		KO30		KO80		KO900	
Calcination Conditions	He	CO$_2$	He	CO$_2$	He	CO$_2$	He	CO$_2$	He	CO$_2$	He	CO$_2$
X_1	0.79	0.63	0.78	0.66	0.72	0.63	0.73	0.61	0.74	0.59	0.53	0.64
X_{20}	0.62	0.23	0.50	0.22	0.31	0.20	0.26	0.17	0.24	0.15	0.24	0.14
X_r	0.55	0.17	0.42	0.16	0.20	0.14	0.15	0.12	0.15	0.08	0.15	0.07
ΔX_r	0.38		0.26		0.06		0.03		0.07		0.08	
K	0.37	0.44	0.37	0.41	0.29	0.48	0.30	0.56	0.42	0.41	0.32	0.56

Fig. 5. CaO conversion (**X**) as a function of the cycle number (**N**) for CaL tests of limestone of different particle sizes carried out at CSP-He (**a**) and CSP-CO$_2$ (**b**) conditions. Solid lines correspond to best fits of Eq. (2) to the experimental data.
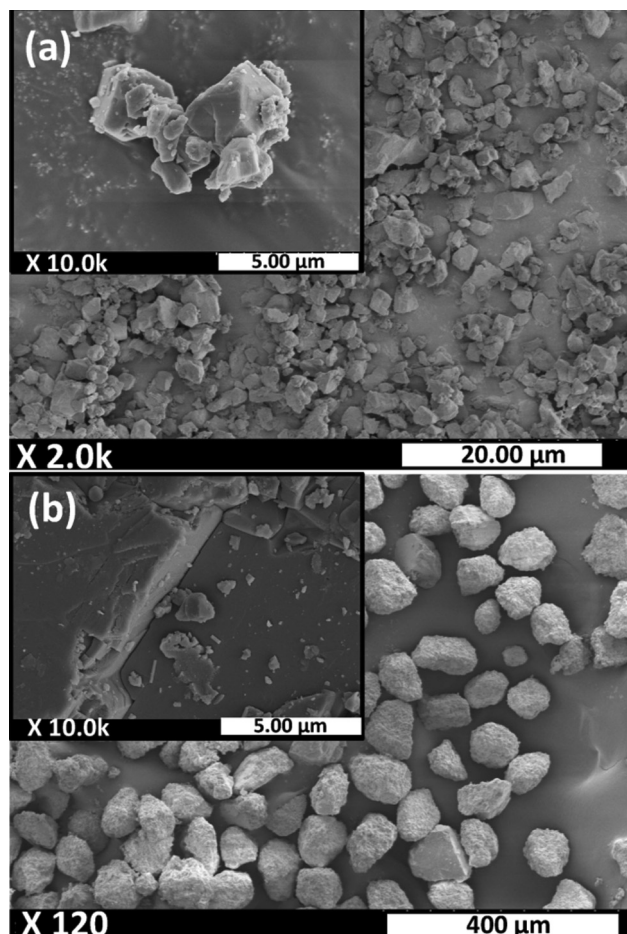
Fig. 6. SEM micrographs illustrating starting (a) KO2 and (b) KO80 particles.

studied by SEM. For comparative purposes, the samples KO2 and KO80 are chosen as representative of very small and large particles respectively. Fig. 6 includes the micrographs of as received limestone. The relatively large particles in KO80 sample appear as non-aggregated individual particles comprising a narrow distribution range. On the other hand, KO2 particles form larger aggregates due to cohesive forces, which for this size are much stronger than the particle weight [51]. In both cases, particles are constituted by well-defined crystals.

SEM micrographs in Fig. 7 shows comparative sequences of the morphological changes undergone by KO2 and KO80 particles during the CaL cycles carried out in CSP-He conditions. The micrographs correspond to the CaO arising after the first calcination stage, the CaCO3 formed in the subsequent recarbonation stage; the CaCO3 formed after 20 cycles and finally the CaO after calcination in the 20th cycle.

CSP-He

KO2 sample, composed of small particles averaging 2 μm, forms sizable aggregates through the entire multicycle experiment. After just one calcination and carbonation stage (Fig. 7a and b respectively) the individual particles can still be distinguished whereas repeating cycles lead to the merging of neighbouring particles into large porous structures (Fig. 7c and d). This morphology, composed of small aggregates, grants the material a remarkable cycling stability. Arguably, this structure proves very resistant to deactivation by pore-plugging, thereby ensuring a high surface area of CaO available for carbonation remains despite repeated cycling (Fig. 7d). In contrast, while KO80 particles leave a relatively porous

structure after the initial carbonation (Fig. 7e), the subsequent carbonation stage leads to the rapid formation of a $CaCO_3$ blocking layer preventing the diffusion of CO_2 molecules to the interior of the particle. Subsequent calcination and carbonation stages eventually lead to the progressive sintering of the surface layer, which is ultimately the only part of the particle that undergoes repeated transformations. Fig. 7g and h show the porous core underneath the sintered surface created by the pore-plugging effect after 20 calcination and carbonation cycles. The grain growth and sintering occur mainly during the carbonation stage as it is promoted by CO_2. Actually, both KO2 and KO80 samples (Fig. 7b and f) evidence considerable grain growth even after the first recarbonation, with the formation of a mosaic structure, comprised of about 1 μm grains covering the entire particle surface. Therefore, the limited grain size observed underneath the external sintered layer in Fig. 7g and h proves the inner core has remained inactive during the cycles. In the inset of Fig. 7h, a fracture is shown to emphasize the marked differences between the surface $CaCO_3$ shell and the inner unreacted CaO core. It should be noted that the inset in Fig. 7h was taken using identical magnification as the main image to better highlight the disparity in grain sizes. Finally, it is interesting how the conversion of $CaCO_3$ into CaO exhibits a shape-memory feature; the shades of the previous $CaCO_3$ grains are apparent in subsequent CaO (Fig. 7g). This shape-memory feature preserves the blocking layer along the carbonation and calcinations cycles and facilitates further sintering, leading to the progressive decay in CaO conversion.

The relationship between these morphological transformations and the multicycle behavior described is Fig. 5a is clear. The relevance of the *pore-plugging* effect depends on particle size; the larger the size, the higher the volume of material that remains inactive underneath the plugging layer. Hence the limited CaO conversion exhibited by the larger particle sizes in the multicycle tests. For smaller particles, a greater fraction of the material contributes to conversion each carbonation stage. Furthermore, the CaO arising from the calcination of the mosaic-like sintered structure shows a significant loss of surface porosity (Fig. 7g) with respect the starting material (Fig. 7a) leading to a decay in CaO conversion along ensuing cycles. Table 3 includes the BET surface area values measured for KO2 and KO80 samples after one calcination and after 5 carbonation and calcination cycles. As expected, there is a reduction in surface area because of sintering after a few cycles. Surface available for carbonation decreases about 30% in the case of the small KO2 particles whereas the reduction reaches 50% for the larger KO80 particles. That difference can be attributed to the formation of the sintered surface layer. It is also interesting that the surface area for all 4 samples studied is quite similar after the first calcination.

CSP-CO_2

As it will be discussed hereafter, sample behaviour is remarkably different when cycled in CSP-CO_2 conditions, due to the harsher calcination conditions; pure CO_2 and a high temperature of 950 °C. The overall effect on the multicycle conversion is a worsening of cycling performance with respect to CSP-He conditions, especially in the case of smaller particles. The sequence shown in Fig. 8a–d illustrate how small KO2 particles cycled in CSP-CO_2 conditions endure progressive aggregation, eventually leading to the formation of a macroporous structure constituted of merged neighbouring grains. Also, while in $CaCO_3$ form, well developed grains in mosaic structures are clearly distinguished. However, the morphology of subsequent CaO exhibits striking features that contrast with what previously observed in CSP-He. Instead of preserving the mosaic structure attained by $CaCO_3$ grains in the preceding carbonation stage, CaO arising in CSP-CO_2 conditions constitutes a macroporous globular structure containing large
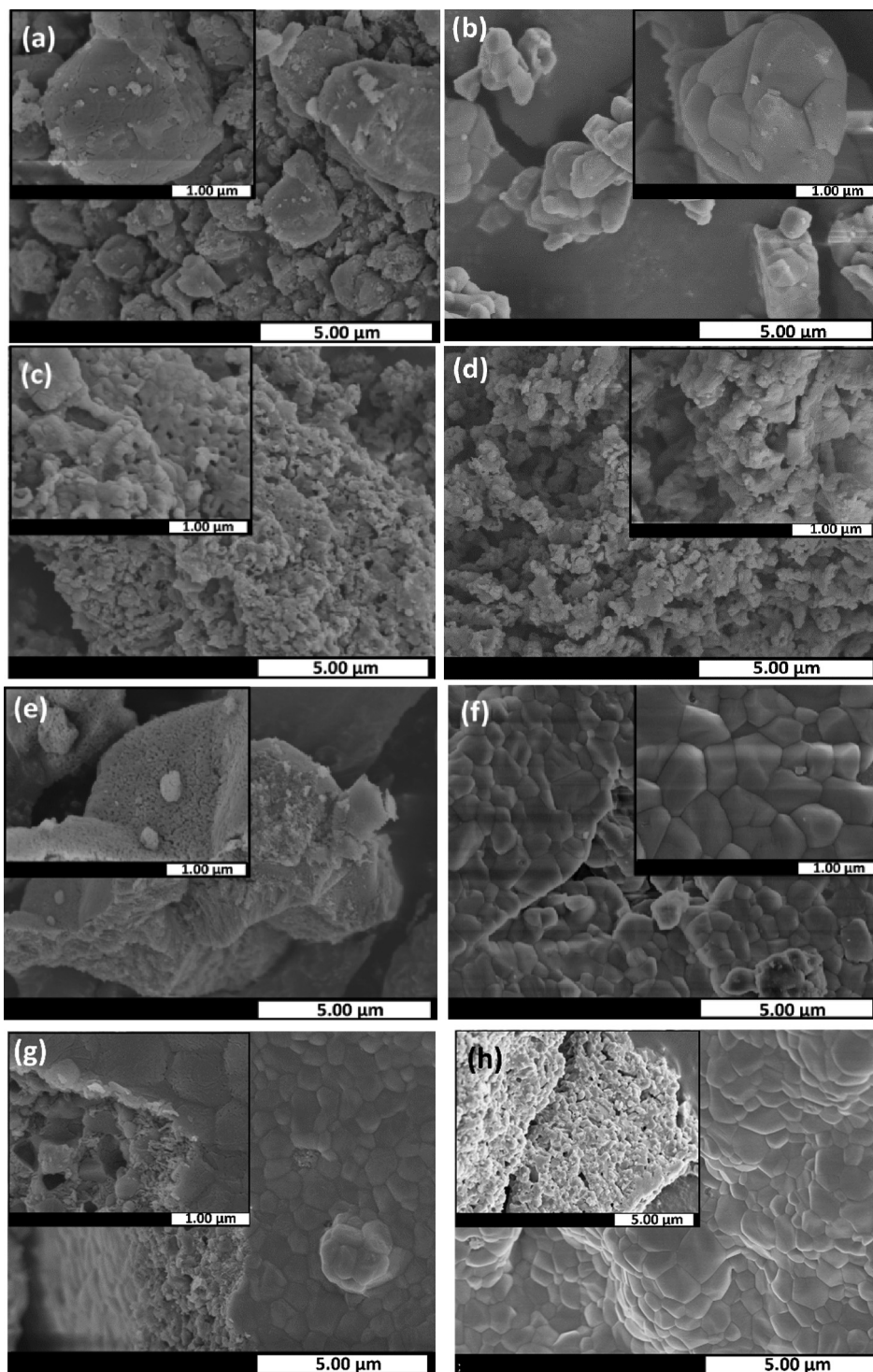
Fig. 7. SEM micrographs illustrating morphology changes during carbonation and calcination cycles in CSP-He conditions for limestone samples KO2 and KO80. (a) KO2 CaO after first calcination; (b) KO2 $CaCO_3$ after the first recarbonation; (c) KO2 CaO after 20 cycles, (d) KO2 $CaCO_3$ after 20 cycles, (e) KO80 CaO after first calcination; (f) KO80 $CaCO_3$ after the first recarbonation; (g) KO80 CaO after 20 cycles and (h) KO80 $CaCO_3$ after 20 cycles.

channels. Moreover, no differences in morphology were observed between the surface and the interior of the particles. Thus, it seems that pore-plugging phenomenon is not that relevant in this CSP-CO_2 operation scheme as the formation of macroporous channels largely prevents the particles to be completely covered by the clogging carbonate layer. This arrangement is a consequence of the high temperatures attained, well over $CaCO_3$ Tamman temperature

(about 500 °C), that strongly promote mass transfer by solid state diffusion [52]. That, coupled with the grain-growth promoting effect of CO_2 lead to extensive sintering all over the entire particle volume. In the case of samples with small average size, neighbouring particles merge as seen in Fig. 8c and 8d. After 20 carbonation and calcination cycles, the loss of surface area is substantial as observed in the insets of Fig. 8c and g. The surface of the CaO

Table 3

BET Surface area measured for KO2 and KO80 samples in CaO form after 1 calcination and after 5 carbonation/calcination cycles. Both CSP-He and CSP-CO_2 reaction conditions were tested.

Sample	S_{BET} (m^2/g)	
	1 calcination	5 carb/calc cycles
KO2-He	14.9	10.2
KO2-CO_2	11.3	6.8
KO80-He	16.3	8.5
KO80-CO_2	15.3	3.9

appears smooth (Fig. 8d and h) in contrast with the cracked surface evidenced in samples cycled in CSP-He (Fig. 7d and h). The progressive loss of micro and mesoporosity in CaO formed under CSP-CO_2 after repeated cycling might explain the reduction in relative weight of the fast reaction-controlled carbonation in relation to the diffusion-controlled carbonation. Besides, as illustrated in Fig. 4, decarbonation rate is at least five times faster at 950 °C in CO_2 than at 750 °C in helium. Sudden release of occluded gases in short times within a high mobility matrix might induce the for-
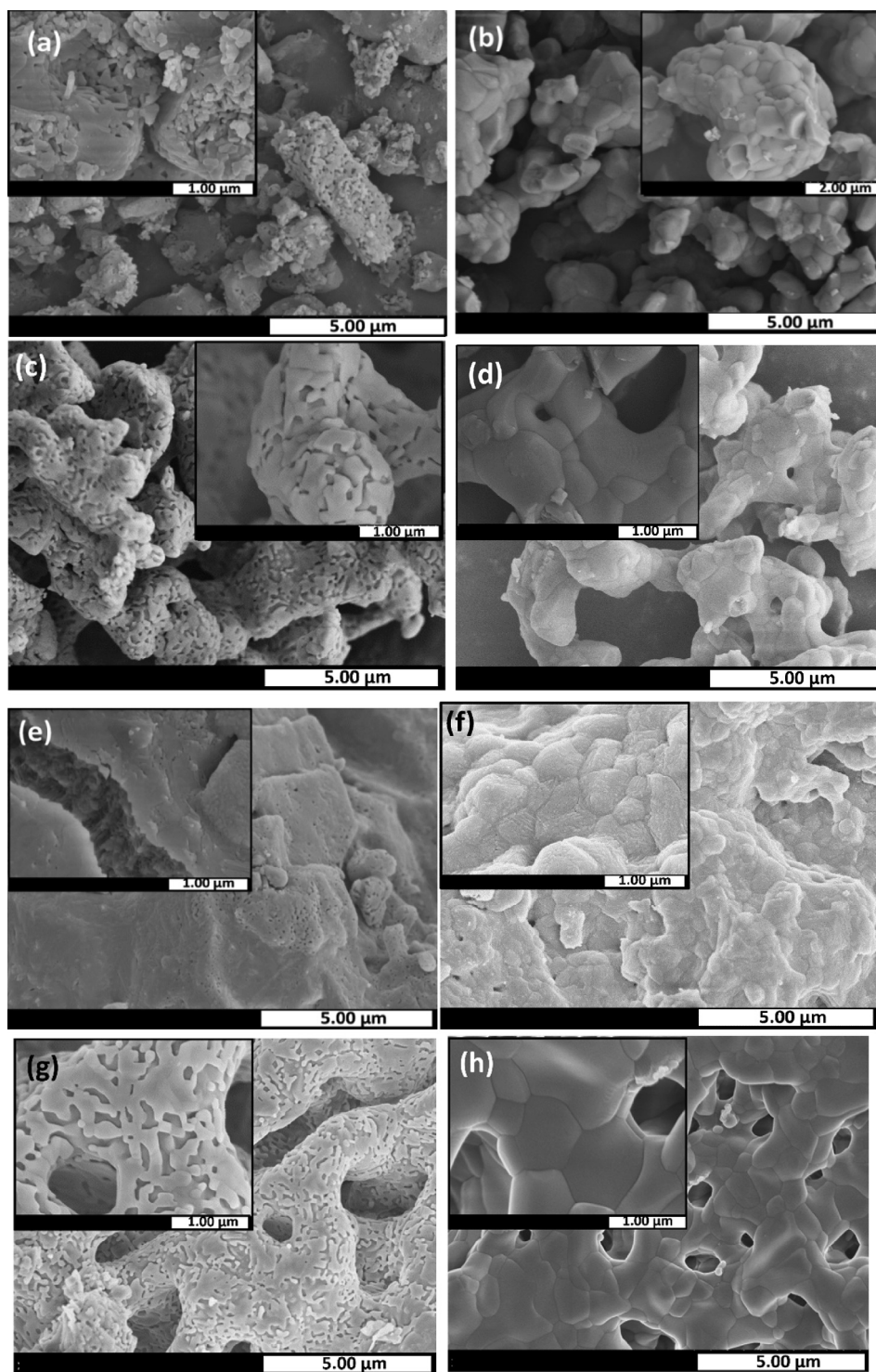

Fig. 8. SEM micrographs illustrating morphology changes during carbonation and calcination cycles in CSP-CO_2 conditions for limestone samples KO2 and KO80. (a) KO2 CaO after first calcination; (b) KO2 $CaCO_3$ after the first recarbonation; (c) KO2 CaO after 20 cycles, (d) KO2 $CaCO_3$ after 20 cycles, (e) KO80 CaO after first calcination; (f) KO80 $CaCO_3$ after the first recarbonation; (g) KO80 CaO after 20 cycles and (h) KO80 $CaCO_3$ after 20 cycles.

mation of a globular-like or foamy structure, as it has been observed in a somewhat different systems, such as the pyrolysis of rice husk to form SiO_2 [53]. Contrary to what occurs in the case of CSP-He, under CSP-CO_2 operation conditions there is little advantage in using small-sized particles since the extensive sintering and particle merging rapidly destroy the relatively open structure displayed in CSP-He (Fig. 7b and d). Table 3 also includes the BET surface area values measured for KO2 and KO80 samples after one calcination and after 5 carbonation and calcination cycles in these experimental conditions. As it occurred in the previous CSP-He conditions, the decline in surface area after 5 consecutive carbonation and calcination reactions is more marked in larger particles, amounting to 75% and 40% for KO80 and KO2 samples respectively.

Conclusions

In this work, the influence of particle size on limestone multicycle chemical looping conversion has been studied under operation conditions relevant for thermochemical energy storage applications. Experimental multicycle tests have been carried out using calcination in helium at relatively low temperatures and calcination at high temperatures in 100% CO_2. Limestone particles of well-defined and narrow particle size distributions have been employed in the analysis. When calcination is carried out in helium at low temperature, the CaO conversion is substantially better for small particles as they are more resilient to pore-plugging, the main deactivation mechanism in CSP-He. Nevertheless, the enhancement is only substantial for particles below 15 µm, which might be difficult to employ in industrial applications involving fluidised bed reactors. Over that size, the formation of a blocking $CaCO_3$ layer on the particles surface prevents further diffusion of CO_2 to the inner particle core. Thus, a substantial volume of material remains inactive during the carbonation stage thereby limiting CaO conversion. On the other hand, when calcination is carried out in CO_2 at high temperatures, the deactivation of the material can be attributed to severe sintering all over the entire particle volume and the loss of surface porosity. Consequently, the improvement in conversion achieved by using particles with small average size is very limited. For particle sizes over 15 µm, the multicycle performance is relatively similar regardless the operation conditions. Thus, the CSP-CO_2 scheme of closed loop might be more advantageous for techno-economic reasons due to the high cost of helium and the simplicity of design. It has also been found that the carbonation process in CSP-He is mostly driven by fast kinetically controlled reaction while in CSP-CO_2 conditions solid-state diffusion has a relevant contribution. The residual CaO conversion attained in our experiments for particle-size usable at industrial level is still below 0.4, the critical value to make the technology competitive with respect to molten salts. Nevertheless, the sequence of morphological changes here presented brings valuable insight into the deactivation mechanism and can provide researchers a guide regarding the type of macroporous structures to be sought in order to minimise the sorbent deactivation.

Compliance with ethics requirements

This article does not contain any studies with human or animal subjects.

Declaration of Competing Interest

The authors have declared no conflict of interest.

Acknowledgements

References

[1] Jiang X, Guan D. Determinants of global CO2 emissions growth. Appl Energy 2016;184:1132–41.

[2] Su M et al. Greenhouse gas emission accounting for EU member states from 1991 to 2012. Appl Energy 2016;184:759–68.

[3] Pietzcker RC et al. Using the sun to decarbonize the power sector: The economic potential of photovoltaics and concentrating solar power. Appl Energy 2014;135:704–20.

[4] Fernández AG et al. Mainstreaming commercial CSP systems: a technology review. Renew Energy 2019;140:152–76.

[5] Weinstein LA et al. Concentrating solar power. Chem Rev 2015;115 (23):12797–838.

[6] Chen X et al. State of the art on the high-temperature thermochemical energy storage systems. Energy Convers Manage 2018;177:792–815.

[7] Pardo P et al. A review on high temperature thermochemical heat energy storage. Renew Sustain Energy Rev 2014;32(Supplement C):591–610.

[8] Carrillo AJ et al. Solar energy on demand: a review on high temperature thermochemical heat storage systems and materials. Chem Rev 2019;119 (7):4777–816.

[9] Bonk A et al. Advanced heat transfer fluids for direct molten salt line-focusing CSP plants. Prog Energy Combust Sci 2018;67:69–87.

[10] Fernández ÁG, Cabeza LF. Molten salt corrosion mechanisms of nitrate based thermal energy storage materials for concentrated solar power plants: a review. Sol Energy Mater Sol Cells 2019;194:160–5.

[11] Liu M et al. Review on concentrating solar power plants and new developments in high temperature thermal energy storage technologies. Renew Sustain Energy Rev 2016;53:1411–32.

[12] André L, Abanades S, Flamant G. Screening of thermochemical systems based on solid-gas reversible reactions for high temperature solar thermal energy storage. Renew Sustain Energy Rev 2016;64(Supplement C):703–15.

[13] Prieto C et al. Review of technology: thermochemical energy storage for concentrated solar power plants. Renew Sustain Energy Rev 2016;60:909–29.

[14] Ortiz C et al. The calcium-looping (CaCO3/CaO) process for thermochemical energy storage in concentrating solar power plants. Renew Sustain Energy Rev 2019;113:109252.

[15] Teng L et al. Modified Ca-Looping materials for directly capturing solar energy and high-temperature storage. Energy Storage Mater 2019.

[16] Chacartegui R et al. Thermochemical energy storage of concentrated solar power by integration of the calcium looping process and a CO2 power cycle. Appl Energy 2016;173(Supplement C):589–605.

[17] Blamey J et al. The calcium looping cycle for large-scale CO2 capture. Prog Energy Combust Sci 2010;36(2):260–79.

[18] Benitez-Guerrero M et al. Multicycle activity of natural CaCO3 minerals for thermochemical energy storage in Concentrated Solar Power plants. Sol Energy 2017;153(Supplement C):188–99.

[19] Erans M, Manovic V, Anthony EJ. Calcium looping sorbents for CO2 capture. Appl Energy 2016;180(Supplement C):722–42.

[20] Sunku Prasad J et al. A critical review of high-temperature reversible thermochemical energy storage systems. Appl Energy 2019;254:113733.

[21] Tregambi C et al. An experimental characterization of Calcium Looping integrated with concentrated solar power. Chem Eng J 2018;331:794–802.

[22] Chen X et al. The role of sensible heat in a concentrated solar power plant with thermochemical energy storage. Energy Convers Manage 2019;190:42–53.

[23] Astolfi M, De Lena E, Romano MC. Improved flexibility and economics of calcium looping power plants by thermochemical energy storage. Int J Greenhouse Gas Control 2019;83:140–55.

[24] Ho CK. A review of high-temperature particle receivers for concentrating solar power. Appl Therm Eng 2016;109:958–69.

[25] Salaudeen SA, Acharya B, Dutta A. CaO-based CO2 sorbents: a review on screening, enhancement, cyclic stability, regeneration and kinetics modelling. J CO2 Util 2018;23:179–99.

[26] Grasa GS, Abanades JC. CO2 capture capacity of CaO in long series of carbonation/calcination cycles. Ind Eng Chem Res 2006;45(26):8846–51.

[27] Borgwardt RH. Calcium oxide sintering in atmospheres containing water and carbon dioxide. Ind Eng Chem Res 1989;28(4):493–500.

[28] Valverde JM et al. Role of looping-calcination conditions on self-reactivation of thermally pretreated CO2 sorbents based on CaO. Energy Fuels 2013;27 (6):3373–84.

[29] Alvarez D, Abanades JC. Pore-size and shape effects on the recarbonation performance of calcium oxide submitted to repeated calcination/recarbonation cycles. Energy Fuels 2005;19(1):270–8.

[30] Benitez-Guerrero M et al. Large-scale high-temperature solar energy storage using natural minerals. Sol Energy Mater Sol Cells 2017;168(Supplement C):14–21.

[31] Alvarez D, Abanades JC. Determination of the critical product layer thickness in the reaction of CaO with CO_2. Ind Eng Chem Res 2005;44(15):5608–15.

[32] Sarrion B et al. On the multicycle activity of natural limestone/dolomite for thermochemical energy storage of concentrated solar power. Energy Technology 2016.

[33] Sarrión B et al. Role of calcium looping conditions on the performance of natural and synthetic Ca-based materials for energy storage. J CO2 Util 2018;28:374–84.

[34] Sarrion B et al. Pressure effect on the multicycle activity of natural carbonates and a Ca/Zr composite for energy storage of concentrated solar power. ACS Sustain Chem Eng 2018;6(6):7849–58.

[35] Biasin A, Segre CU, Strumendo M. CaCO3 crystallite evolution during CaO carbonation: critical crystallite size and rate constant measurement by in-situ synchrotron radiation X-ray powder diffraction. Cryst Growth Des 2015;15 (11):5188–201.

[36] Khinast J et al. Decomposition of limestone: the influence of CO_2 and particle size on the reaction rate. Chem Eng Sci 1996;51(4):623–34.

[37] Sánchez Jiménez PE et al. High-performance and low-cost macroporous calcium oxide based materials for thermochemical energy storage in concentrated solar power plants. Appl Energy 2019;235:543–52.

[38] Ma X et al. Preparation of a morph-genetic CaO-based sorbent using paper fibre as a biotemplate for enhanced CO2 capture. Chem Eng J 2019;361:235–44.

[39] Khosa AA, Zhao CY. Heat storage and release performance analysis of CaCO3/CaO thermal energy storage system after doping nano silica. Sol Energy 2019;188:619–30.

[40] Valverde JM, Sanchez-Jimenez PE, Perez-Maqueda LA. Relevant influence of limestone crystallinity on CO_2 capture in the Ca-Looping technology at realistic calcination conditions. Environ Sci Technol 2014;48(16):9882–9.

[41] Grasa GS et al. Reactivity of highly cycled particles of CaO in a carbonation/calcination loop. Chem Eng J 2008;137(3):561–7.

[42] Grasa G et al. Application of the random pore model to the carbonation cyclic reaction. AIChE J 2009;55(5):1246–55.

[43] Behar O, Khellaf A, Mohammedi K. A review of studies on central receiver solar thermal power plants. Renew Sustain Energy Rev 2013;23(Supplement C):12–39.

[44] Zhao B, Su Y, Zhang J. Simulation of gas flow pattern and separation efficiency in cyclone with conventional single and spiral double inlet configuration. Chem Eng Res Des 2006;84(12 A):1158–65.

[45] Valverde JM, Quintanilla MAS. Attrition of Ca-based CO2-adsorbents by a high velocity gas jet. AIChE J 2013;59(4):1096–107.

[46] Arias B et al. Demonstration of steady state CO_2 capture in a 1.7 MWth calcium looping pilot. Int J Greenhouse Gas Control 2013;18:237–45.

[47] Strohle J et al. Carbonate looping experiments in a 1 MWth pilot plant and model validation. Fuel 2014;127:13–22.

[48] Shi H et al. Effect of particle size and cohesion on powder yielding and flow. Kona Powder Part J 2018:advpub.

[49] Sun Z et al. Ionic diffusion through Calcite ($CaCO_3$) layer during the reaction of CaO and CO_2. Chem Eng Sci 2012;81:164–8.

[50] Valverde JM et al. CO_2 multicyclic capture of pretreated/doped CaO in the Ca-looping process. Theory and experiments. PCCP 2013;15(28): 11775–93.

[51] Castellanos A, Valverde JM, Quintanilla MAS. Aggregation and sedimentation in gas-fluidized beds of cohesive powders. Phys Rev E 2001;64(4):041304.

[52] Merkle R, Maier J. On the Tammann-rule. Z Anorg Allg Chem 2005;631(6–7):1163–6.

[53] Vlaev LT, Markovska IG, Lyubchev LA. Non-isothermal kinetics of pyrolysis of rice husk. Thermochim Acta 2003;406(1–2):1–7.